



Delft University of Technology

## Rapid single-shot parity spin readout in a silicon double quantum dot with fidelity exceeding 99%

Takeda, Kenta; Noiri, Akito; Nakajima, Takashi; Camenzind, Leon C.; Kobayashi, Takashi; Sammak, Amir; Scappucci, Giordano; Tarucha, Seigo

### DOI

[10.1038/s41534-024-00813-0](https://doi.org/10.1038/s41534-024-00813-0)

### Publication date

2024

### Document Version

Final published version

### Published in

NPJ Quantum Information

### Citation (APA)

Takeda, K., Noiri, A., Nakajima, T., Camenzind, L. C., Kobayashi, T., Sammak, A., Scappucci, G., & Tarucha, S. (2024). Rapid single-shot parity spin readout in a silicon double quantum dot with fidelity exceeding 99%. *NPJ Quantum Information*, 10(1), Article 22. <https://doi.org/10.1038/s41534-024-00813-0>

### Important note

To cite this publication, please use the final published version (if applicable).  
Please check the document version above.

### Copyright

Other than for strictly personal use, it is not permitted to download, forward or distribute the text or part of it, without the consent of the author(s) and/or copyright holder(s), unless the work is under an open content license such as Creative Commons.

### Takedown policy

Please contact us and provide details if you believe this document breaches copyrights.  
We will remove access to the work immediately and investigate your claim.

## ARTICLE OPEN



# Rapid single-shot parity spin readout in a silicon double quantum dot with fidelity exceeding 99%

Kenta Takeda<sup>1</sup>✉, Akito Noiri<sup>1</sup>, Takashi Nakajima<sup>1</sup>, Leon C. Camenzind<sup>1</sup>, Takashi Kobayashi<sup>2</sup>, Amir Sammak<sup>3,4</sup>, Giordano Scappucci<sup>3,5</sup> and Seigo Tarucha<sup>1,2</sup>✉

Silicon-based spin qubits offer a potential pathway toward realizing a scalable quantum computer owing to their compatibility with semiconductor manufacturing technologies. Recent experiments in this system have demonstrated crucial technologies, including high-fidelity quantum gates and multiqubit operation. However, the realization of a fault-tolerant quantum computer requires a high-fidelity spin measurement faster than decoherence. To address this challenge, we characterize and optimize the initialization and measurement procedures using the parity-mode Pauli spin blockade technique. Here, we demonstrate a rapid (with a duration of a few  $\mu\text{s}$ ) and accurate (with >99% fidelity) parity spin measurement in a silicon double quantum dot. These results represent a significant step forward toward implementing measurement-based quantum error correction in silicon.

npj Quantum Information (2024)10:22; <https://doi.org/10.1038/s41534-024-00813-0>

## INTRODUCTION

High-fidelity measurement of quantum states is crucial for the operation of a quantum computer. This is particularly important for quantum error correction protocols, which rely on feedback quantum gates that are based on syndrome measurements<sup>1,2</sup>. In order to implement these protocols effectively, the qubit measurements must be performed much faster than decoherence. While previous experiments with spin qubits in silicon have achieved significant milestones such as quantum non-demolition measurement<sup>3,4</sup>, high-fidelity quantum gates<sup>5–9</sup>, and multi-qubit control<sup>10–12</sup>, single-shot measurement of single-spin states has generally been slow and with modest fidelity. The readout of a single-spin state typically relies on spin-to-charge conversion techniques, such as energy-selective tunneling<sup>13</sup> or Pauli spin blockade (PSB)<sup>14,15</sup>. The energy-selective readout requires high bandwidth measurement with long duration to detect stochastic tunneling events with various time scales. While this scheme has been employed for demonstrations of high-fidelity single-spin readout in the literature, the readout is typically orders of magnitude slower than phase coherence times<sup>9,16</sup>. On the other hand, the PSB readout utilizes spin-selective tunneling between two quantum dots. In this case, the signal results from a stationary difference of charge states, and charge discrimination is much easier.

## RESULTS AND DISCUSSION

### Device and charge stability diagram

Here, we demonstrate that it is possible to perform a parity mode spin readout with a fidelity well above 99% with the PSB mechanism. Our sample incorporates a micromagnet for electric-dipole spin resonance<sup>17</sup> and two-qubit CZ gate<sup>18</sup>. It creates a large Zeeman energy difference that causes fast relaxation of the unpolarized triplet state ( $T_0$ ), resulting in the parity mode PSB readout<sup>19</sup>. While this parity mode PSB readout has been utilized before in silicon/silicon-germanium (Si/SiGe)<sup>11</sup> and silicon metal–semiconductor–oxide systems<sup>20,21</sup>, high-fidelity readout

within the phase coherence time has not been reported. In this study, with improvements in the charge sensing performance and pulse engineering to reduce state mapping error, we show the high-fidelity spin readout can be performed within 3  $\mu\text{s}$  which is considerably faster than the average spin echo coherence times of around 100  $\mu\text{s}$ . Coherent Rabi oscillations show a visibility approaching 99.6% (or a state preparation and measurement (SPAM) fidelity of 99.8%), compatible with measurement-based quantum error detection and correction protocols.

Figure 1a shows a scanning electron microscope image of our device. The overlapping aluminum gates<sup>22</sup> are fabricated on top of an isotopically enriched Si/SiGe wafer (heterostructure B in<sup>23</sup>). From our previous devices<sup>7,10</sup>, the gate geometry is modified to increase the sensitivity of the charge sensor quantum dot to the inter-dot transitions. First, the charge sensor is more asymmetrically coupled to the quantum dots to be measured. Second, we have decreased the distance between the quantum dots and the charge sensor because the sensitivity drops significantly as this distance increases<sup>22</sup>. The sample is cooled down in a dilution refrigerator, and an external magnetic field of 0.5 T is applied. In this work, we form two quantum dot spin qubits  $Q_L$  and  $Q_R$ , under gates P3 and P4, respectively, while the left part of the device serves as an extended reservoir for  $Q_L$ . Gate B3 is used to control the tunnel coupling between the left reservoir and  $Q_L$ , and gate B4 is used to control the inter-dot tunnel coupling  $t_c$ . We monitor the occupancy of the double quantum dot by a nearby charge sensor quantum dot (indicated by the upper circle in Fig. 1a). The conductance of the charge sensor is measured by a radio-frequency reflectometry technique<sup>24,25</sup> with a bandwidth of approximately 10 MHz, which is limited by the quality factor of the tank circuit. In what follows, we use virtual gate voltages (vB3, vP3, vB4, vP4) to individually control quantum dot potential and tunnel coupling<sup>26</sup>. The single-qubit manipulation is realized by an electric-dipole spin resonance (EDSR) technique using a micromagnet<sup>17</sup>. The qubit manipulation is performed at the charge symmetry point, where the qubit energy is first-order insensitive

<sup>1</sup>RIKEN Center for Emergent Matter Science (CEMS), Wako, Japan. <sup>2</sup>RIKEN Center for Quantum Computing (RQC), Wako, Japan. <sup>3</sup>QuTech, Delft University of Technology, Delft, The Netherlands. <sup>4</sup>Netherlands Organisation for Applied Scientific Research (TNO), Delft, The Netherlands. <sup>5</sup>Kavli Institute of Nanoscience, Delft University of Technology, Delft, The Netherlands. ✉email: [kenta.takeda@riken.jp](mailto:kenta.takeda@riken.jp); [tarucha@riken.jp](mailto:tarucha@riken.jp)

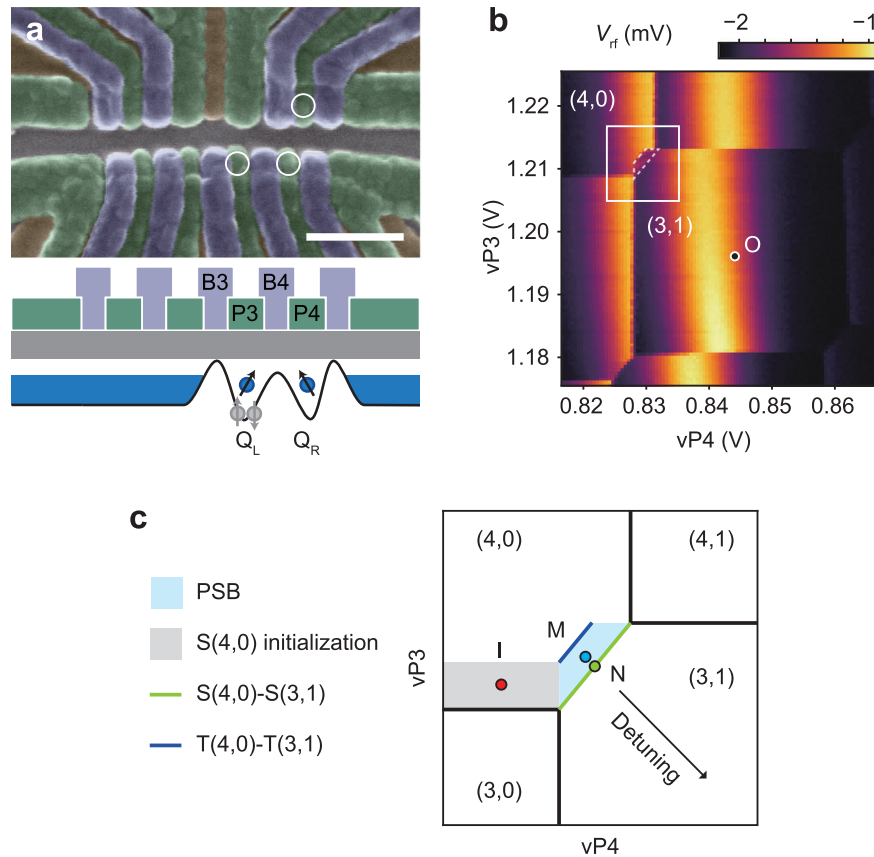


**Fig. 1 Device and charge stability diagram.** **a** False-colored scanning electron microscope image of the device. The green, purple, and brown gates correspond to plunger/accumulation, barrier, and screening gates, respectively. The lower channel is used for defining the right and left quantum dots under the plunger gates P3 and P4 (lower panel). A micromagnet is fabricated on top of the fine gate stack. The right quantum dot in the upper channel is used as a charge sensor quantum dot. The right bath for the charge sensor is connected to a radio frequency tank circuit. The white circles indicate where quantum dots are formed. The scale bar is 200 nm. **b** Charge stability diagram for the four-electron configuration.  $V_{rf}$  is the reflectometry signal from the charge sensor. The  $vP4$  voltage sweep is performed from right to left so that the triplet (3,1) state is latched in the spin blockade regime. The dashed white trapezoidal region indicates where the latching due to PSB occurs. The point O (black circle in the (3,1) configuration) indicates the charge symmetry point where the qubit operation is performed. **c** Zoom in schematic stability diagram around the (4,0)–(3,1) charge degeneracy point. The red, blue, and green points show the plunger gate configurations for initialization (I), measurement (M), and inter-dot transition (N). The right blue area shows the configuration where PSB occurs. The gray area shows that energy-selective tunneling to  $S(4,0)$  occurs. The green (blue) line around the border of the PSB region shows the inter-dot transition for the singlet (triplet) states. The detuning is defined as  $vP4 - vP3$ .

to detuning charge noise<sup>27,28</sup>. The residual exchange coupling is measured to be 21 kHz (see Supplementary Fig. 1).

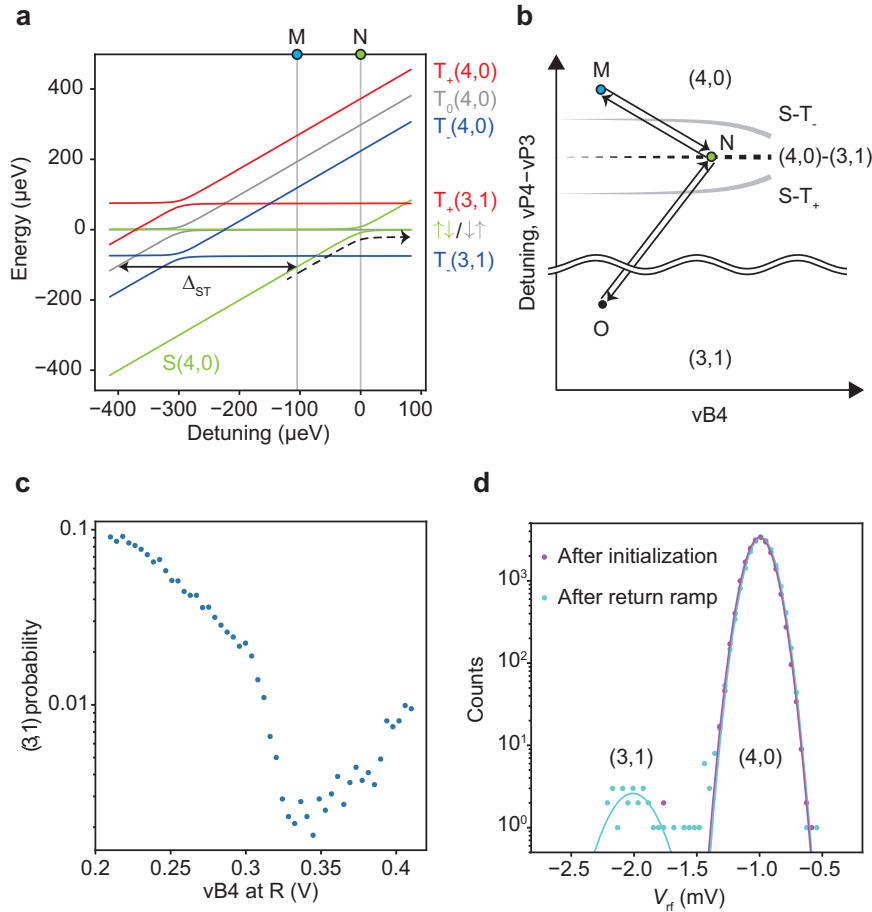
We use the four-electron charge states (4,0) and (3,1) for the PSB readout, where  $(n_L, n_R)$  denotes the number of electrons in the left and right quantum dots. For the (4,0) configuration, the first excited state is energetically split by the orbital splitting rather than the valley splitting<sup>11</sup>. This results in a larger readout window since the orbital excitation energy (400  $\mu$ eV for the four-electron state) is larger than the valley splitting (100–150  $\mu$ eV in this device). In Fig. 1b, we measure a charge stability diagram as a function of  $vP3$  and  $vP4$ . We rapidly ramp  $vP4$  from the (3,1) configuration towards the (4,0) configuration, causing the (3,1) triplet state to latch in the PSB regime. We choose an integration time of 10  $\mu$ s per point to ensure that relaxation of the triplet state is not significant. The PSB regime appears as an extended trapezoidal region showing a (3,1) charge signal within the (4,0) configuration (see inside the white rectangle in Fig. 1b).

### PSB pulse scheme and state mapping error

The first step of spin initialization is energy-selective tunneling to the (4,0) singlet state  $S(4,0)$ . It is performed by pulsing  $vP3$  and  $vP4$  to move near the (3,0)–(4,0) boundary and waiting for 5  $\mu$ s (I

in Fig. 1c). We simultaneously pulse  $vB3$  to increase the dot-to-reservoir tunnel rate, enhancing the initialization speed. Here, the singlet-triplet excitation energy is much larger than the thermal broadening ( $\sim 300$   $\mu$ eV vs.  $\sim 4$   $\mu$ eV), resulting in a negligible population of higher excited states. After initializing to  $S(4,0)$ , we pulse  $vP3$ ,  $vP4$ , and  $vB3$  to return to the measurement configuration at M.

The second step is a rapid adiabatic passage from  $S(4,0)$  and  $|\uparrow\downarrow\rangle$  (3,1), as illustrated by the dashed black arrow in Fig. 2a. For spin qubits with a micromagnet, the primary concern in this procedure is the adiabatic transition through the  $S - T_-$  anti-crossing. The size of this anti-crossing is determined by the magnetic field gradient and  $t_c$ , with only the latter being well-controllable through gate voltages. For high-fidelity state mapping and measurement, we need to consider the following aspects: small  $t_c$  for long  $T_1$  in the PSB regime and  $S - T_-$  diabaticity, and large  $t_c$  for adiabatic inter-dot transition. To achieve this, we pulse the detuning ( $vP3 - vP4$ ) and barrier ( $vB4$ ) voltages as in Fig. 2b. In addition to the detuning ramp for navigating the charge state, we introduce a pulse to the barrier gate to increase  $t_c$  when crossing the inter-dot transition while maintaining  $t_c$  reasonably small for the  $S - T_-$  transition (N in



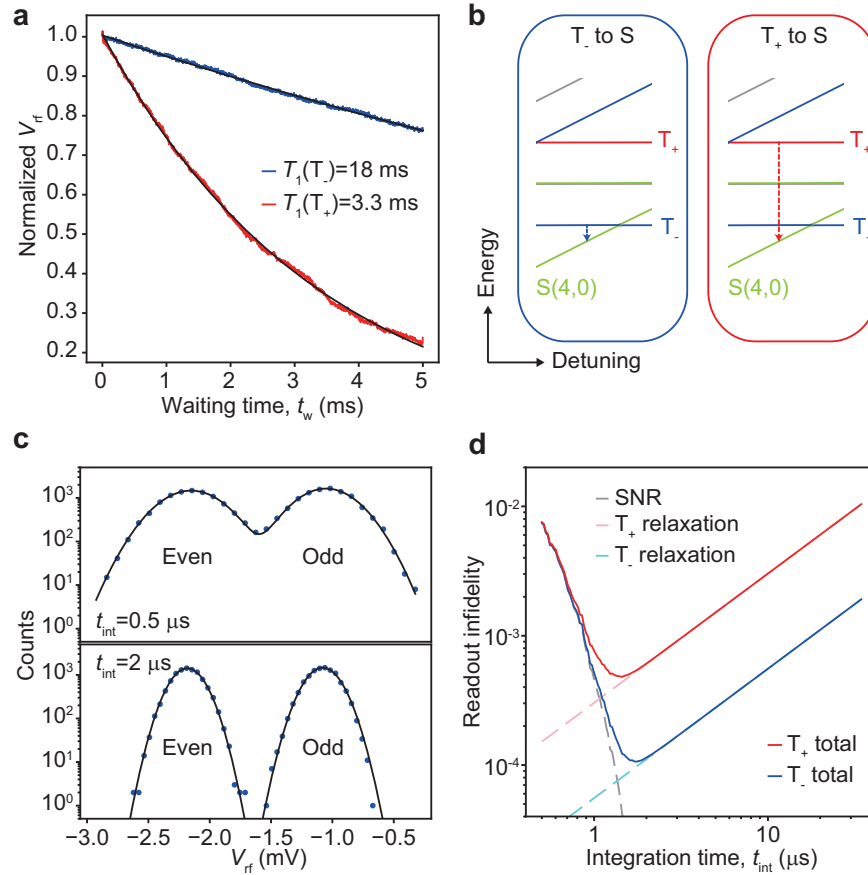
**Fig. 2 Initialization procedure.** **a** Energy diagram of the two-electron states around the inter-dot charge transition. The zero detuning point is defined as the  $S(4,0)$ – $S(3,1)$  degeneracy point. The vertical gray lines show the detuning parameters corresponding to points M and N. The point O resides at the charge symmetry point at a large detuning (see Fig. 1b). The dashed line represents the ideal rapid adiabatic passage for initializing  $|\uparrow\downarrow\rangle$ . We use parameters  $\Delta_{ST} = 400$  μeV, average Zeeman energy of 18 GHz, Zeeman energy difference of 100 MHz, and  $t_c = 2$  GHz for the illustration. **b** Schematic of initialization pulse trajectory in the  $vB4$ -detuning plane. The durations are 15 ns (ramp time from M to N), 15 ns (waiting time at N), and 100 ns (ramp time from N to O). The position of  $S - T_{\pm}$  crossings is illustrated for  $t_c$  changing exponentially as a function of  $vB4$  (solid gray lines). **c** Measurement of even parity return probability as a function of the virtual barrier gate voltage  $vB4$  at N. **d** Histograms of the charge sensor signal for 10,000 shots of measurement after the  $S(4,0)$  initialization and after pulsing to O and directly returning to M. The solid lines show a fitting to a Gaussian function. The (3,1) counts for the configuration right after initialization are too small to fit.

Fig. 2a, b). After crossing the inter-dot transition, the state is pulsed deep into the Coulomb blockade regime for single-qubit manipulation (O in Fig. 1b). Here, we pulse the detuning and  $vB4$  to adiabatically decrease the exchange coupling (see Supplementary Fig. 2). After the qubit manipulation at O, we perform a projective measurement by a reverse pulse sequence (from O to M), and the charge discrimination is performed at M.

Experimentally, we observe the second part (adiabatic rapid passage) limits the overall SPAM fidelity. To optimize the pulse condition, we measure the (3,1) return probability as a function of  $vB4$  at N (Fig. 2b). As no spin manipulation is performed at O, the final state ideally remains the same as the original state. However, too large  $vB4$  leads to adiabatic transition to  $T_-$  or too small  $vB4$  leads to diabatic inter-dot transition, causing a finite (3,1) charge signal. For the optimal  $vB4$ , we obtain approximately 0.2% (3,1) probability after pulsing to and directly returning from O (Fig. 2c). In Fig. 2d, we show a comparison of the readout outcomes for the states right after  $S(4,0)$  initialization and after returning from O. We observe that, while the  $S(4,0)$  initialization error is negligible, an excursion to the (3,1) operation point results in an increased error count.

### Relaxation time, SNR, and readout fidelity

In the PSB regime, there exist three possible spin-blocked states:  $T_-$ ,  $T_+$ , and  $|\uparrow\downarrow\rangle$ . Among these three states,  $|\uparrow\downarrow\rangle$  quickly mixes with the unblocked  $|\uparrow\downarrow\rangle$  state via the micro-magnet field gradient ( $T_1 = 141 \pm 8$  ns, see Supplementary Fig. 3). As a result, in practice, only the spin-polarized triplet states  $T_-$  and  $T_+$  are blocked, and the readout is the so-called parity readout. In Fig. 3a, b, we show the measurement of the  $T_1$  relaxation times of triplet states  $T_-$  and  $T_+$ . These two triplet states are prepared by applying a  $\pi$  rotation to  $|\uparrow\downarrow\rangle$ . We obtain  $T_1 = 18.2 \pm 0.2$  (3.268  $\pm$  0.001) ms for  $T_-$  ( $T_+$ ) by fitting the data to exponential decay. These long  $T_1$  values are achieved by reducing  $t_c$  during the readout (see Supplementary Fig. 4). While the field-gradient components causing the spin relaxation are similar in magnitude for these two cases, there are several possible mechanisms that cause this difference. For example, the respective detuning parameters for the relevant spin-flipping anti-crossings ( $S(4,0) - T_{\pm}$ ) are different for these two states, and the associated energy differences being compensated by phonons, charge noise, and/or Johnson-Nyquist noise also differ<sup>29,30</sup>. In addition for the case of  $T_+$ , sequential relaxation via the unpolarized spin states may occur. Pinpointing the exact



**Fig. 3 Relaxation, SNR, and readout fidelity.** **a** Relaxation times. The blue (red) trace shows the measurement result for the initial state  $T_-$  ( $T_+$ ). The data is obtained by normalizing the measured  $V_{rf}$  so that  $V_{rf}(t_w = 0) = 1$  and  $V_{rf}(t_w = \infty) = V_{rf}(S(4, 0)) = 0$ . The  $S(4, 0)$  signal is obtained by measuring  $V_{rf}$  at M directly after the initialization. The solid black lines are the exponential fit curves  $V_{rf}(t_w) = V_0 \exp(-t_w/T_1)$ , where  $V_0 \sim 1$  is the fitting parameter to account for the signal contrast. **b** Zoom up of the energy diagram plotted with relevant relaxation channels (left panel:  $T_-$  to S, right panel:  $T_+$  to S). **c** Histograms for two different measurement integration times  $t_{int} = 0.5 \mu s$  and  $2 \mu s$ . The blue points show histogram counts for measured data. The solid black lines show fitting to a double Gaussian function. **d** Infidelities as a function of  $t_{int}$ . The SNR-inferred infidelity is calculated from the overlap of two Gaussian peaks, and the  $T_1$ -inferred infidelity is defined as  $1 - \exp(-t_{int}/T_1)$ .

mechanisms limiting these  $T_1$  values, including additional experiments on parametric dependence and related theory, is a subject for future study. Nonetheless, these are both long enough for high-fidelity parity spin measurement.

Next, we move on to characterizing the signal-to-noise ratio (SNR), which is another important metric for spin readout. Figure 3c shows the results of charge discrimination after preparing an equal superposition of  $|\uparrow\downarrow\rangle$  and  $T_-$ . Two peaks in each histogram correspond to even and odd parity readout outcomes. If the integration time  $t_{int}$  is too short, the overlap of two Gaussian peaks causes a substantial infidelity (upper panel in Fig. 3c). However, if  $t_{int}$  is too long, the relaxation of excited (3,1) state reduces the readout fidelity. The optimal  $t_{int}$  to minimize readout infidelity is obtained by balancing these two factors. Figure 3d plots the readout infidelity taking into account both  $T_1$  and SNR. For both  $T_-$  and  $T_+$ , we obtain measurement infidelities below 0.1% with  $t_{int} = 2 \mu s$ . For experiments requiring measurement-based feedback, it might be important to reduce  $t_{int}$  further to minimize the dephasing of idling qubits. For reduced  $t_{int} = 0.5 \mu s$ , the infidelities are higher but remain below 1%.

### Spin qubit control and SPAM fidelity

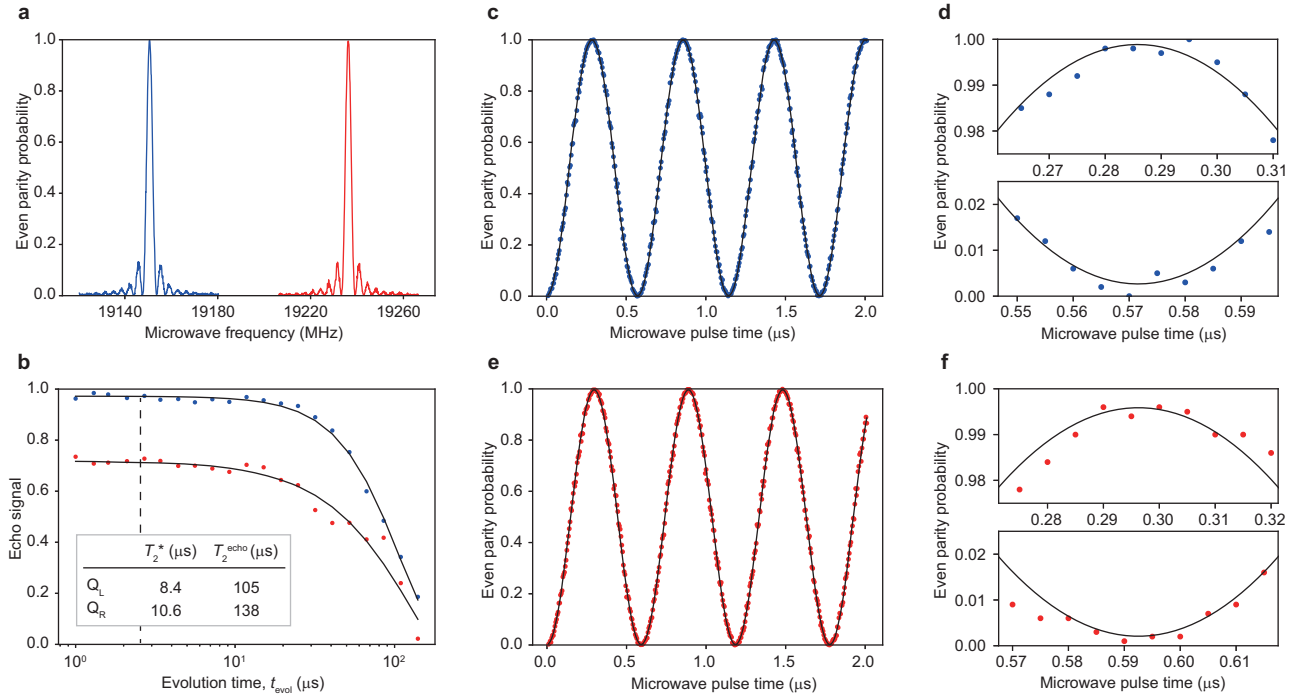
Finally, we assess the SPAM fidelity by measuring coherent Rabi oscillations. Throughout these experiments, we use  $t_{int} = 3 \mu s$ . In

Fig. 4a, we measure two resonance peaks for  $Q_L$  and  $Q_R$ , with a difference in resonance frequencies corresponding to a Zeeman energy difference of  $\Delta E_z = 85.6$  MHz. The Rabi frequency is chosen so that the amplitude of the off-resonant drive of the idle qubit is negligibly small. We measure Rabi oscillations by varying the microwave pulse time  $t_p$  (Fig. 4b, c). We find that the Rabi oscillation decay is negligible, and the oscillation visibilities are well above 99% for both qubits ( $99.6 \pm 0.2\%$  for  $T_-$  and  $99.4 \pm 0.2\%$  for  $T_+$ ). For the  $T_-$  readout, the 0.2% initialization error due to the adiabatic  $S - T_-$  transition limits the visibility. For the  $T_+$  readout, the  $T_1 \sim 3$  ms accounts for  $\sim 0.1\%$  of the additional visibility loss as compared with the case for  $T_-$ . We speculate that the additional 0.1% of infidelity comes from a larger adiabatic transition probability through the  $S - T_+$  anti-crossing where  $vB_4$  is larger than the  $S - T_-$  anti-crossing, as seen in the pulse shape of Fig. 2b. A more complex pulse to reduce  $t_c$  when crossing both degeneracy points could circumvent this problem.

### Readout duration and phase coherence time

For implementing measurement-based quantum protocols that require phase coherence, the total duration of readout is also crucial. More explicitly, measurement has to be faster than relevant  $T_2$ , not only  $T_1$ . Our spin qubits have  $T_2^* \sim 8 \mu s$  (see





**Fig. 4 Spin qubit control and SPAM fidelity.** **a** EDSR spectra of two spin qubits. The blue (red) trace shows the measured data of  $Q_L$  ( $Q_R$ ). The resonance frequencies are 19.1506 GHz for  $Q_L$  and 19.2362 GHz for  $Q_R$ . **b** Spin echo measurements. The evolution time refers to the total duration of waiting time between microwave pulses. The blue (red) points show the measured data of  $Q_L$  ( $Q_R$ ). The black lines show the fit with exponential decay  $P(t_{\text{evol}}) = V \exp(-(t_{\text{evol}}/T_2^{\text{echo}})^{\gamma})$  from which we extract  $T_2^{\text{echo}} = 105 \pm 1(138 \pm 8) \mu\text{s}$ ,  $\gamma = 1.89 \pm 0.07(1.3 \pm 0.1)$ , and  $V = 0.972 \pm 0.002(0.969 \pm 0.002)$  for  $Q_L$  ( $Q_R$ ). The data points and fit curve for  $Q_R$  are offset by  $-0.25$  for clarity. The non-ideal visibility is due to the imperfect calibration of microwave pulses. The dashed black line represents  $t_{\text{evol}} = 2.4 \mu\text{s}$ . **c** Rabi oscillation of  $Q_L$ . The blue points are measured data, and the black line is a sinusoidal fit. **d** Zoom up of a peak and dip in (c). **e**, **f** Measurements similar to c and d, but for  $Q_R$ .

Supplementary Fig. 5), and these inhomogeneous phase coherence times can be extended to above  $100 \mu\text{s}$  using a single refocusing  $\pi$  pulse (Fig. 4b). On the other hand, the overall duration of our measurement procedure can be as short as  $2.4 \mu\text{s}$  ( $0.13 \mu\text{s}$  ramp time +  $0.25 \mu\text{s}$  reflectometry signal rise time +  $2 \mu\text{s}$  integration time). When comparing this duration to the typical loss of coherence expected from the Hahn echo decay of  $Q_L$  and  $Q_R$ , we expect less than a 1% loss of phase coherence during the measurement ( $0.1\%$  ( $0.5\%$ ) for  $Q_L$  ( $Q_R$ )). While combining the spin echo sequence and the PSB readout needs additional steps accounting for the phase shift induced by the micromagnet field gradient and voltage pulses for state mapping (see Supplementary Note 6 for details), our result suggests that, with an appropriate device and experimental configuration, it is possible to perform a single-spin qubit readout precisely and fast enough while maintaining phase information.

In conclusion, we have demonstrated high-fidelity parity PSB readout for electron spin qubits in a silicon double quantum dot. The readout fidelities compare favorably to the best values in other spin qubit platforms<sup>16,31,32</sup>. The visibility of Rabi oscillation is mainly limited by spin state mapping. This could be improved by further optimization of both pulse shape and speed. The readout duration is much shorter than the spin echo dephasing time. We note that the implemented parity spin readout does not preserve the original eigenstates, unlike the standard ZZ parity measurement, and we need a designated measurement ancilla quantum dot to readout a single-spin state. It may suggest that optimizing only the  $T_-$  readout is sufficient for applications where we need single-spin projective measurement. Overall, our results suggest that it is possible to perform a single-spin readout in a time scale where the phase coherence of idling qubits is well preserved, and

it may open the door toward realizing measurement-based quantum error detection or correction protocols in silicon.

## METHODS

The sample is cooled down in a dilution refrigerator. The electron temperature is estimated to be around 45 mK by observation of the thermal broadening of the charge transition line. The charge sensor quantum dot is connected to an LC tank circuit with an inductance of  $1.2 \mu\text{H}$  (CoilCraft 1206CS-122X) and a resonance frequency of 181 MHz. The rf carrier signal is generated by an internal AWG of a Keysight M3302A module running at  $500 \text{MSa s}^{-1}$ . The signal is attenuated and applied to the device via a directional coupler mounted at the mixing chamber plate of the dilution refrigerator. The reflected signal is first amplified by a Cosmic microwave CITLF2 cryogenic amplifier and further amplified by room temperature amplifiers. The amplified signal is then digitized by the M3302A module at a sampling rate of  $500 \text{MSa s}^{-1}$ . Its internal FPGA is used to demodulate the signal to the baseband voltage  $V_{\text{rf}}$ . The gate electrodes P3, P4, B3, and B4 are connected to a Keysight M3302A AWG module running at  $1 \text{GSa s}^{-1}$  via cryogenic bias-tees. The outputs of the AWG module are filtered with Mini Circuits SBLP-39+ Bessel low-pass filters. The microwave signal is generated by two Keysight E8267D vector signal generators that are IQ modulated by a Keysight M3302A module. Unless noted, we collect 1000 single-shot measurement outcomes to obtain an even parity probability.

## DATA AVAILABILITY

The data used to produce the figures in this work is available from the Zenodo repository at <https://doi.org/10.5281/zenodo.10473513>.

Received: 18 July 2023; Accepted: 17 January 2024;  
Published online: 13 February 2024

## REFERENCES

1. Krinner, S. et al. Realizing repeated quantum error correction in a distance-three surface code. *Nature* **605**, 669–674 (2022).
2. Acharya, R. et al. Suppressing quantum errors by scaling a surface code logical qubit. *Nature* **614**, 676–681 (2023).
3. Yoneda, J. et al. Quantum non-demolition readout of an electron spin in silicon. *Nat. Commun.* **11**, 1–7 (2020).
4. Xue, X. et al. Repetitive quantum non-demolition measurement and soft decoding of a silicon spin qubit. *Phys. Rev. X* **10**, 021006 (2020).
5. Yoneda, J. et al. A quantum-dot spin qubit with coherence limited by charge noise and fidelity higher than 99.9%. *Nat. Nanotechnol.* **13**, 102–106 (2018).
6. Yang, C. H. et al. Silicon qubit fidelities approaching incoherent noise limits via pulse engineering. *Nat. Electron.* **2**, 151–158 (2019).
7. Noiri, A. et al. Fast universal quantum gate above the fault-tolerance threshold in silicon. *Nature* **601**, 338–342 (2022).
8. Xue, X. et al. Quantum logic with spin qubits crossing the surface code threshold. *Nature* **601**, 343–347 (2022).
9. Mills, A. R. et al. Two-qubit silicon quantum processor with operation fidelity exceeding 99%. *Sci. Adv.* **8**, eabn5130 (2022).
10. Takeda, K., Noiri, A., Nakajima, T., Kobayashi, T. & Tarucha, S. Quantum error correction with silicon spin qubits. *Nature* **608**, 682–686 (2022).
11. Philips, S. G. J. et al. Universal control of a six-qubit quantum processor in silicon. *Nature* **609**, 919–924 (2022).
12. Weinstein, A. J. et al. Universal logic with encoded spin qubits in silicon. *Nature* **615**, 817–822 (2023).
13. Elzerman, J. M. et al. Single-shot read-out of an individual electron spin in a quantum dot. *Nature* **430**, 431–435 (2004).
14. Ono, K., Austing, D. G., Tokura, Y. & Tarucha, S. Current rectification by Pauli exclusion in a weakly coupled double quantum dot system. *Science* **297**, 1313–1317 (2002).
15. Johnson, A. C. et al. Triplet-singlet spin relaxation via nuclei in a double quantum dot. *Nature* **435**, 925–928 (2005).
16. Keith, D. et al. Benchmarking high fidelity single-shot readout of semiconductor qubits. *N. J. Phys.* **21**, 063011 (2019).
17. Tokura, Y., Van Der Wiel, W. G., Obata, T. & Tarucha, S. Coherent single electron spin control in a slanting zeeman field. *Phys. Rev. Lett.* **96**, 1–4 (2006).
18. Meunier, T., Calado, V. E. & Vandersypen, L. M. K. Efficient controlled-phase gate for single-spin qubits in quantum dots. *Phys. Rev. B* **83**, 1–4 (2011).
19. Seedhouse, A. E. et al. Pauli blockade in silicon quantum dots with spin-orbit control. *PRX Quantum* **2**, 010303 (2021).
20. Yang, C. H. et al. Silicon quantum processor unit cell operation above one Kelvin. *Nature* **580**, 350–354 (2020).
21. Niegemann, D. J. et al. Parity and singlet-triplet high-fidelity readout in a silicon double quantum dot at 0.5 K. *PRX Quantum* **3**, 040335 (2022).
22. Zajac, D. M., Hazard, T. M., Mi, X., Nielsen, E. & Petta, J. R. Scalable gate architecture for densely packed semiconductor spin qubits. *Phys. Rev. Appl.* **054013**, 1–8 (2016).
23. Paquelet Wuetz, B. et al. Reducing charge noise in quantum dots by using thin silicon quantum wells. *Nat. Commun.* **14**, 1385 (2023).
24. Noiri, A. et al. Radio-frequency detected fast charge sensing in undoped silicon quantum dots. *Nano Lett.* **20**, 947–952 (2020).
25. Connors, E. J., Nelson, J. J. & Nichol, J. M. Rapid high-fidelity spin-state readout in Si/Si-Ge quantum dots via rf reflectometry. *Phys. Rev. Appl.* **13**, 24019 (2020).
26. Baart, T. A. et al. Single-spin CCD. *Nat. Nanotechnol.* **11**, 330–334 (2016).
27. Martins, F. et al. Noise suppression using symmetric exchange gates in spin qubits. *Phys. Rev. Lett.* **116**, 116801 (2016).
28. Reed, M. D. et al. Reduced sensitivity to charge noise in semiconductor spin qubits via symmetric operation. *Phys. Rev. Lett.* **116**, 110402 (2016).
29. Huang, P. & Hu, X. Spin relaxation in a Si quantum dot due to spin-valley mixing. *Phys. Rev. B* **90**, 235315 (2014).
30. Borjans, F., Zajac, D. M., Hazard, T. M. & Petta, J. R. Single-spin relaxation in a synthetic spin-orbit field. *Phys. Rev. Appl.* **10**, 1 (2018).
31. Mills, A. R. et al. High-fidelity state preparation, quantum control, and readout of an isotopically enriched silicon spin qubit. *Phys. Rev. Appl.* **18**, 064028 (2022).
32. Blumoff, J. Z. et al. Fast and high-fidelity state preparation and measurement in triple-quantum-dot spin qubits. *PRX Quantum* **3**, 10352 (2022).

## ACKNOWLEDGEMENTS

We acknowledge Xin Liu and Reiko Kuroda for assistance with sample fabrication. This work was supported financially by JST Moonshot R&D Grant Number JPMJMS226B and JSPS KAKENHI grant Nos. 18H01819, 20H00237, and 23H05455. A.N. acknowledges support from JST PRESTO Grant Number JPMJPR23F8. T.N. acknowledges support from JST PRESTO Grant Number JPMJPR2017. L.C.C. acknowledges support from Swiss NSF Mobility Fellowship No. P2BSP2 200127.

## AUTHOR CONTRIBUTIONS

A.N. fabricated the device. K.T. performed the measurements. A.N., T.N., T.K., and L.C.C. contributed to the data acquisition and discussed the results. A.S. and G.S. developed and supplied the  $^{28}\text{Si}/\text{SiGe}$  heterostructure. K.T. wrote the paper with inputs from all co-authors. S.T. supervised the project.

## COMPETING INTERESTS

The authors declare no competing interests.

## ADDITIONAL INFORMATION

**Supplementary information** The online version contains supplementary material available at <https://doi.org/10.1038/s41534-024-00813-0>.

**Correspondence** and requests for materials should be addressed to Kenta Takeda or Seigo Tarucha.

**Reprints and permission information** is available at <http://www.nature.com/reprints>

**Publisher's note** Springer Nature remains neutral with regard to jurisdictional claims in published maps and institutional affiliations.



**Open Access** This article is licensed under a Creative Commons Attribution 4.0 International License, which permits use, sharing, adaptation, distribution and reproduction in any medium or format, as long as you give appropriate credit to the original author(s) and the source, provide a link to the Creative Commons license, and indicate if changes were made. The images or other third party material in this article are included in the article's Creative Commons license, unless indicated otherwise in a credit line to the material. If material is not included in the article's Creative Commons license and your intended use is not permitted by statutory regulation or exceeds the permitted use, you will need to obtain permission directly from the copyright holder. To view a copy of this license, visit <http://creativecommons.org/licenses/by/4.0/>.

© The Author(s) 2024